Osmotically assisted reverse osmosis utilizing hollow fiber membrane module for concentration process

Togo, Norihiro ; Nakagawa, Keizo ; Shintani, Takuji ; Yoshioka, Tomohisa ; Takahashi, Tomoki ; Kamio, Eiji ; Matsuyama, Hideto

(Citation)
Industrial & Engineering Chemistry Research,58(16):6721-6729

(Issue Date)
2019-03-28

(Resource Type)
journal article

(Version)
Accepted Manuscript

Osmotically assisted reverse osmosis utilizing hollow fiber membrane module for concentration process

Norihiro Togo[1], Keizo Nakagawa[1], Takuji Shintani[1], Tomohisa Yoshioka[1], Tomoki Takahashi[2], Eiji Kamio[2], and Hideto Matsuyama[1,2]**

[1]Center for Membrane and Film Technology, Graduate School of Science, Technology, and Innovation, Kobe University, 1-1 Rokkodai, Nada, Kobe 657-8501, Japan

[2]Center for Membrane and Film Technology, Department of Chemical Science and Engineering, Kobe University, 1-1 Rokkodai, Nada, Kobe 657-8501, Japan

Keywords:

concentration process, osmotically assisted reverse osmosis; hollow fiber membrane module; cellulose triacetate membrane; concentration polarization

Table of Contents

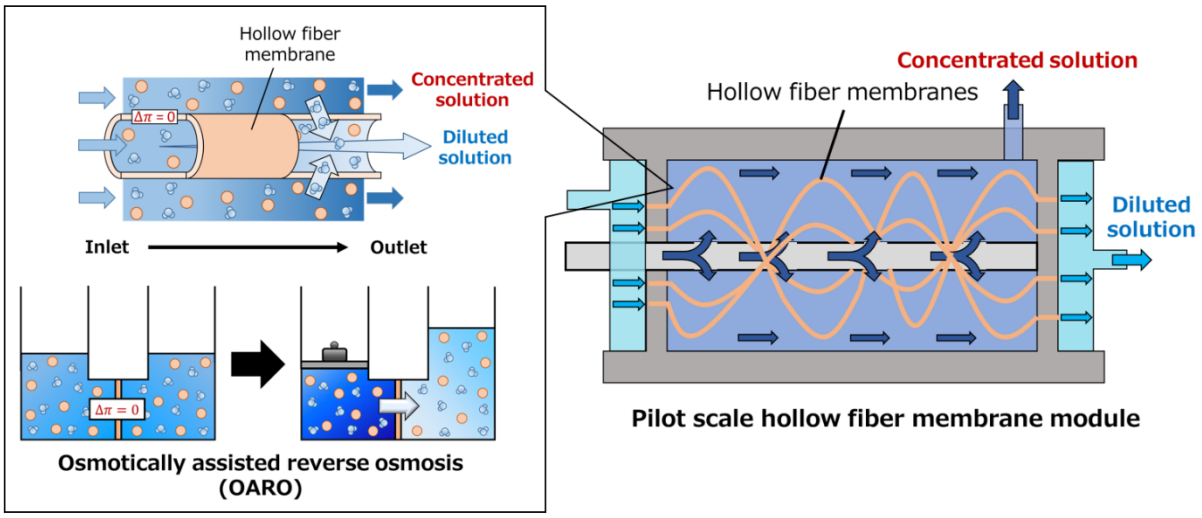

Abstract

Solution concentration processes such as evaporation, freeze concentration, and reverse osmosis are commonly used in food processing and environmental applications. However, these processes are frequently examined to lower energy costs and improve concentration ratios. This study performed concentration tests and theoretical calculations for osmotically assisted reverse osmosis (OARO) using a pilot scale hollow fiber membrane module. In the concentration test using NaCl solution, water flux and concentration ratio were measured with changing flow rate, concentration, and applied pressure. Water permeation and solution concentration were achieved, even using concentrated salt solutions (0.5 and 1.0 M), with applied pressure of 8–12 bar, which was lower than the osmotic pressure (25 bar for 0.5 M NaCl; 50 bar for 1.0 M NaCl). The calculation results were in good agreement with the experimental results and the validity of the calculation model was confirmed. Analysis revealed that the concentration gradient and concentration polarization in the module changed with operating conditions and these factors affected the water flux and the concentration ratio.

1. Introduction

Concentration technology is currently used in food preparation and environmental applications.[1] For example, concentration technology is important in fruit juice processing to control product quality and transport costs.[2] The commonly used concentration technologies are evaporation, freeze concentration, and reverse osmosis (RO). Evaporation and freeze concentration can achieve high concentration, but can incur high energy and equipment costs. However, RO has the advantage of lower energy requirements when compared with the two abovementioned methods because RO does not need phase changes.[3–5] In addition, thermal damage to the solute is not a cause for concern because RO is performed at low temperature.[2,6] However, RO has a low concentration ratio[7] when compared with the evaporation method. According to a report on the concentration of fruit juice, RO can condense up to about only half of that achieved by the evaporation method.[8] The hydraulic pressure must be able to overcome the osmotic pressure of the solution in the RO process. In the case of solution with high osmotic pressure, the operating pressure becomes quite high. However, when the pressure resistance of the polymer membrane is not high enough, the applied pressure should be limited, and this compromises concentration by the RO method. For these reasons, alternative way that can achieve high concentration with low energy consumption is required.

Very recently, osmotically assisted reverse osmosis (OARO) was proposed as a new concentration technique.[9–13] The OARO process, which is schematically illustrated in Fig. 1, is also known as draw solution-assisted reverse osmosis (DSARO),[9] osmotically enhanced dewatering-reverse osmosis (OED-RO),[11] or cascading osmotically mediated reverse osmosis (COMRO).[10] In this process, it is important to supply solutions of equal concentration on each side of the semipermeable membrane. There is no osmotic pressure difference between the solutions

separated by the membrane, but water permeates according to the applied pressure from one side to the other and concentration is promoted regardless of the concentration of the feed solution. Therefore, the OARO process not only allows concentration of high-osmotic-pressure solution that cannot be used in conventional RO, but also reduces energy costs and inhibits membrane damage induced by applied pressure. Furthermore, there is no need for high-pressure-resistant material for pipes and modules, and reductions in equipment costs can be expected. OARO has the advantages of high water recovery and low reverse solute diffusion.[9–13] Thus, to put OARO into practical use, it is necessary to investigate the scale-up process and assess its feasibility. There are several pilot scale membrane module types that can operate with different membrane structures and filling methods. These modules have been studied in other membrane processes such as RO, pressure retarded osmosis (PRO), and forward osmosis (FO).[14–20] However, testing of the OARO process using pilot scale membrane modules has not been investigated to date.

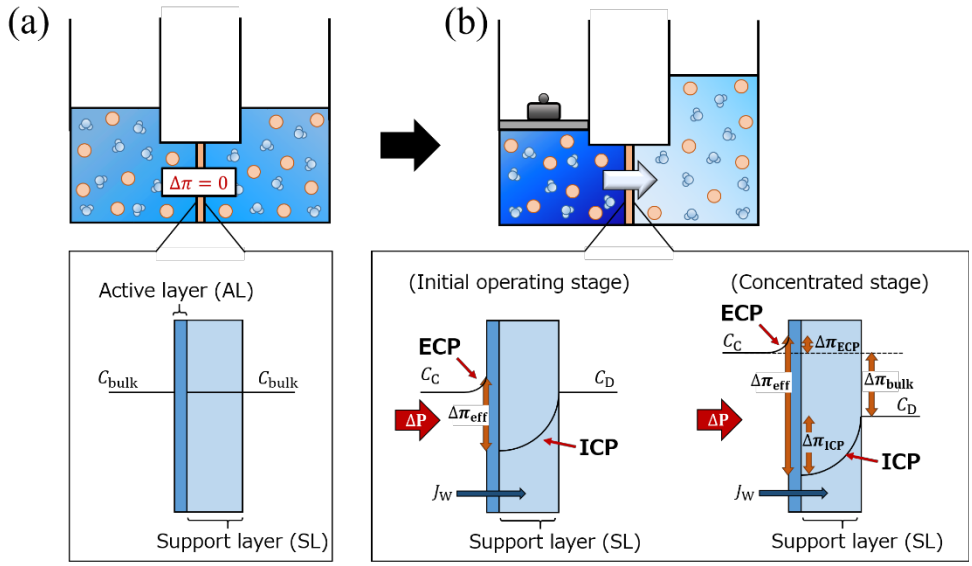

Figure 1 Schematic diagram of the OARO process and concentration polarization, (a) without applied pressure, and (b) initial operating stage (left) and concentrated stage (right).

In this research, we conducted fundamental studies of OARO using a cellulose triacetate (CTA) 5-inch hollow fiber membrane module, which is widely used in Middle Eastern seawater desalination plants.[21] These tests investigated the influences of operating conditions such as flow rate, concentration of feed solution, and applied pressure on concentration ratio and water flux. Furthermore, we analyzed the concentration gradient and concentration polarization in the module using a theoretical calculation model based on the module structure.

2. Theory

2.1. Permeability model in OARO

Figure 1 shows a schematic diagram of the OARO process. Solutions of the same concentration are supplied to both sides of the semipermeable membrane (Fig. 1 (a)). Initially, there is no osmotic pressure difference between the solutions. Therefore, water permeates when pressure is applied on one side regardless of the feed solution concentration (Fig. 1 (b)). Both external and internal concentration polarizations, which are important for water permeation,[22–24] were considered for the water and solute permeation model. In this work, the CTA membrane contained of an active layer (AL) with separation function and a support layer (SL). At the interface of the active layer, water permeates across and salt is rejected. Then, a solute concentration increase called external concentration polarization (ECP) occurs at the active layer surface. However, the solution is diluted by the permeation of water in the support layer. Then the concentration reduction called internal concentration polarization (ICP) occurs. When the osmotic pressure differences caused by ECP and ICP are defined as $\Delta\pi_{\mathrm{ECP}}$ [bar] and $\Delta\pi_{\mathrm{ICP}}$ [bar], respectively, and the bulk osmotic

pressure difference caused by concentration and dilution is defined as $\Delta\pi_{\mathrm{bulk}}$ [bar], the water flux (J_{W} [L·m^{-2}·h^{-1}]) is expressed by the following equation:

$$\begin{aligned} J_{\mathrm{W}} &= A(\Delta P - \Delta\pi_{\mathrm{eff}}) \\ &= A\{\Delta P - (\Delta\pi_{\mathrm{ECP}} + \Delta\pi_{\mathrm{ICP}} + \Delta\pi_{\mathrm{bulk}})\}, \end{aligned} \tag{1}$$

where A [L·m^{-2}·h^{-1}·bar^{-1}] and ΔP [bar] are the water permeability coefficient and the hydraulic pressure difference, respectively. Furthermore, Equation (1) is transformed into the following equation using the relationship of material balance:[12]

$$J_{\mathrm{W}} = A\left[\Delta P - \frac{\pi_{\mathrm{C,b}}\exp\left(\frac{J_{\mathrm{W}}}{k}\right) - \pi_{\mathrm{D,b}}\exp\left(-\frac{J_{\mathrm{W}}S}{D}\right)}{1+\frac{B}{J_{\mathrm{W}}}\left\{\exp\left(\frac{J_{\mathrm{W}}}{k}\right) - \exp\left(-\frac{J_{\mathrm{W}}S}{D}\right)\right\}}\right], \tag{2}$$

where k [L·m^{-2}·h^{-1}] is the mass transfer coefficient in the boundary layer at the active layer surface, $\pi_{\mathrm{C,b}}$ [bar] and $\pi_{\mathrm{D,b}}$ [bar] are the bulk osmotic pressures of concentrated and diluted sides, respectively, S [m] is a structure parameter, D [m^2·h^{-1}] is the solute diffusion coefficient, and B [L·m^{-2}·h^{-1}] is the solute permeability coefficient. In addition, the solute flux (J_{S} [mol·m^{-2}·h^{-1}]) is given by:

$$J_{\mathrm{S}} = \frac{B}{\beta RT}\left(\Delta P - \frac{J_{\mathrm{W}}}{A}\right), \tag{3}$$

where β is the van't Hoff coefficient, R [bar·L·mol^{-1}·K^{-1}] is the gas constant, and T [K] is temperature.

2.2. Water flux and concentration change

Figure 2 shows schematic diagrams of the hollow fiber membrane module used in this study, including the feed flow of the shell side (outside the hollow fiber membrane) and the bore side (inside the hollow fiber membrane) solution in the module. At the center of the module, there is a perforated dispersion pipe, from which the shell side solution is supplied in the radial direction. The hollow fiber membranes are arranged in a cross-wound configuration around the dispersion pipe and the bore side solution is supplied in the axial direction. Because the volume of the pilot scale module is large, the conditions such as concentration, pressure, and flow rate change at each point inside the module. Therefore, as shown in Fig. 3 (a), we divided the module zone into radial and axial directions, and conducted stepwise segmental calculations.[20] The division number was 100 in the radial direction (r) and 100 in the axial direction (z), such that the total division number was 10,000. For a certain section (n, m), the flow rate (Q) and the solute concentration (C) on the shell side and bore side are given by the following equations from the relation of material balance as shown in Fig. 3 (b).

$$Q_{\mathrm{Shell}(n,m+1)} = Q_{\mathrm{Shell}(n,m)} - J_{\mathrm{w}(n,m)} A_{\mathrm{m}(n,m)}, \tag{4}$$

$$Q_{\mathrm{Bore}(n+1,m)} = Q_{\mathrm{Bore}(n,m)} + J_{\mathrm{w}(n,m)} A_{\mathrm{m}(n,m)}, \tag{5}$$

$$C_{\mathrm{Shell}(n,m+1)} = \frac{C_{\mathrm{Shell}(n,m)} Q_{\mathrm{Shell}(n,m)} - J_{\mathrm{S}(n,m)} A_{\mathrm{m}(n,m)}}{Q_{\mathrm{Shell}(n,m+1)}}, \tag{6}$$

$$C_{\mathrm{Bore}(n,m+1)} = \frac{C_{\mathrm{Bore}(n,m)} Q_{\mathrm{Bore}(n,m)} + J_{\mathrm{S}(n,m)} A_{\mathrm{m}(n,m)}}{Q_{\mathrm{Bore}(n+1,m)}}, \tag{7}$$

where Q_{Shell} [L/min] and Q_{Bore} [L/min] are the flow rates of shell side and bore side, respectively, ΔQ [L/min] is the permeated water volume, C_{Shell} [mol·L^{-1}] and C_{Bore} [mol·L^{-1}] are the

concentrations of the shell side and bore side, respectively, and A_{m} [m^2] is the membrane area. The water flux was calculated by the following equation:

$$J_{\mathrm{W}} = \frac{Q_{\mathrm{Bore,Out}} - Q_{\mathrm{Bore,In}}}{A_{\mathrm{m}}}, \tag{8}$$

where $Q_{\mathrm{Bore,Out}}$ [L/min] and $Q_{\mathrm{Bore,In}}$ [L/min] are the flow rates of the bore side outlet and inlet, respectively.

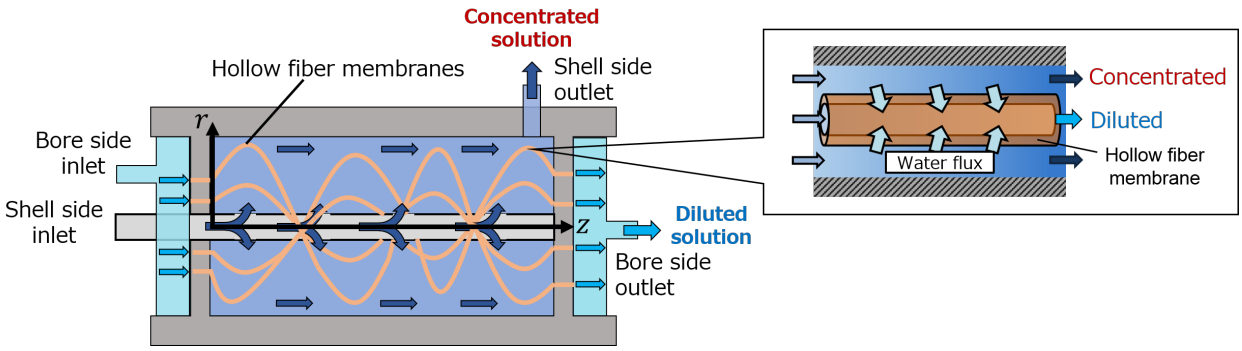

Figure 2 Schematic diagram of hollow fiber membrane module.

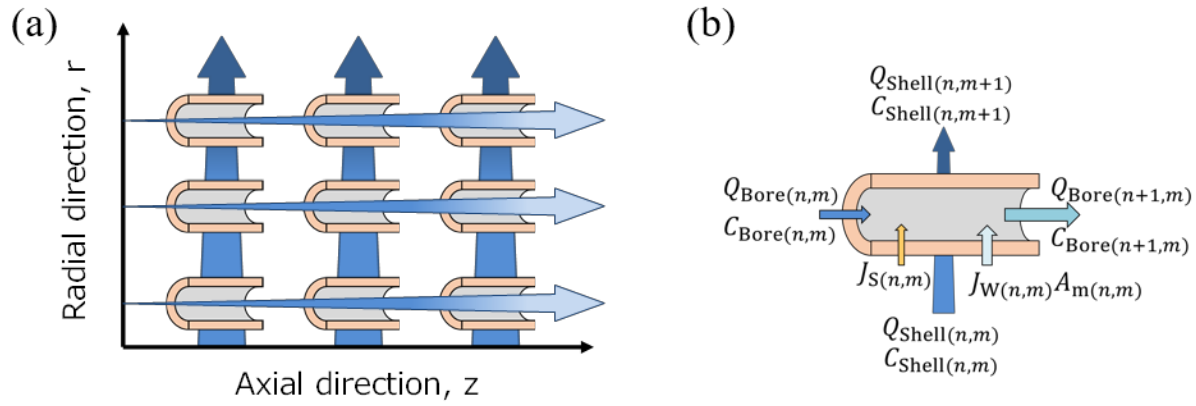

Figure 3 (a) Division calculation method and (b) mass balance in small section.

The influence of the division number in the radial direction and the axial direction on the calculation results of water flux is summarized in Fig. 4. The condition in the calculation is shown in the figure caption. The standard deviations when comparing J_W which is calculated from the division number (r = 100 and z= 100) with those from the division numbers (r = 500 and z= 100) or (r = 100 and z= 500) were 5.4×10^{-4} and 1.2×10^{-3}, respectively. There was little difference in the results of water flux calculated by dividing both radial and axial directions into more than 100 segments. Thus, it was confirmed that a division number of 100 in both radial and axial directions was sufficient.

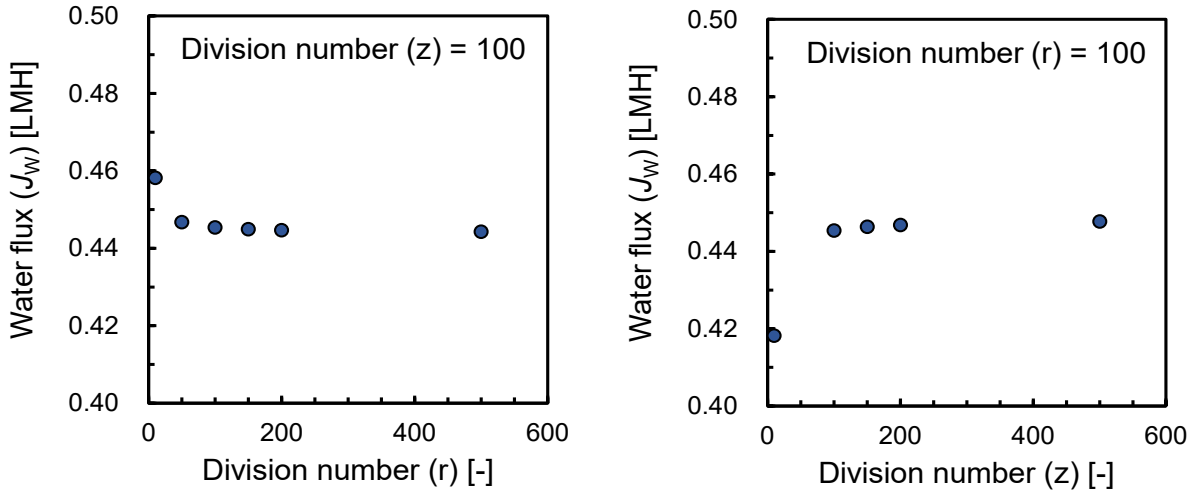

Figure 4 Effect of division number on water flux (Q_{Shell} = 4 L/min, ΔP = 12 bar, C_0 = 1.0 M).

2.3. Pressure drop

The pressure drop in a pilot scale membrane module is an important parameter because it greatly affects the water flux. In particular, the inner diameter of the hollow fiber membrane was very small (85 μm) and the number of membranes installed in the vessel was large (216,720). Therefore, it was necessary to accurately assess the pressure drop across the module. The pressure drop in the 5-inch hollow fiber membrane module used in this study has been reported previously.[18–20] For a certain section (n, m), given that the inside of the hollow fiber membrane has laminar flow, the pressure drop of the bore side (inside of hollow fiber membrane) can be expressed by the following equation using the Hagen-Poiseuille equation:

$$\Delta P_{\mathrm{drop,Bore}(n,m)} = \frac{128\times\mu\times Q_{\mathrm{bore}(n,m)}}{\pi\times F_{\mathrm{N}(n,m)}} \times \left(\frac{1}{d_{\mathrm{mem}}}\right)^4 dz, \quad (9)$$

where μ [bar·min] is viscosity, and $F_{\mathrm{N}}(n, m)$ and d_{mem} [m] are the number and inner diameter of hollow fibers, respectively. However, the pressure drop of the shell side (outside of hollow fiber membrane) is expressed by the following equation using Ergun's equation to cover laminar flow to turbulent flow:

$$\Delta P_{\mathrm{drop,Shell}(n,m)} = \left\{\frac{150\times\sigma^2\times\mu\times u_{\mathrm{Shell}(n,m)}}{(1-\sigma)^3\times(1.5D_{\mathrm{mem}})^2} + \frac{1.75\times\sigma\times\rho\times u^2_{\mathrm{Shell}(n,m)}}{(1-\sigma)^3\times 1.5D_{\mathrm{mem}}}\right\} dr, \quad (10)$$

where σ is the packing density, u_{Shell} [m·min^{-1}] is the linear velocity, D_{mem} [m] is the outer diameter of the hollow fiber, and ρ [kg·m^{-3}] is the solution density.

2.4. Module efficiency (η)

Here, an ideal separation without concentration polarization, pressure drop, and solute permeation through the membrane is considered. When the initial concentration is C_0 [mol/L], the volumes of

the concentrated side and the diluted side are V_{C} [L] and V_{D} [L], respectively, the amounts of substances N_{C} [mol] and N_{D} [mol] are expressed by the following equations:

$$N_{\mathrm{C}} = C_0 \cdot V_{\mathrm{C}}, \tag{11}$$

$$N_{\mathrm{D}} = C_0 \cdot V_{\mathrm{D}}. \tag{12}$$

Here, subscripts (C) and (D) denote the concentrated and diluted sides, respectively. When the pressure (ΔP) is applied and water of ΔV [L] permeates, the concentrations of the concentrated side and diluted side (C_{C} [mol/L] and C_{D} [mol/L]) are expressed by the following equations:

$$C_{\mathrm{C}} = \frac{C_0 \cdot V_{\mathrm{C}}}{V_{\mathrm{C}} - \Delta V}, \tag{13}$$

$$C_{\mathrm{D}} = \frac{C_0 \cdot V_{\mathrm{D}}}{V_{\mathrm{D}} + \Delta V}. \tag{14}$$

According to the van't Hoff equation, the osmotic pressure of the concentrated side and the diluted side (π_{C} [bar] and π_{D} [bar]) and the osmotic pressure difference ($\Delta\pi$ [bar]) are defined by the following equations:

$$\pi_{\mathrm{C}} = \beta C_{\mathrm{C}} RT, \tag{15}$$

$$\pi_{\mathrm{D}} = \beta C_{\mathrm{D}} RT, \tag{16}$$

$$\Delta\pi = \pi_{\mathrm{C}} - \pi_{\mathrm{D}}. \tag{17}$$

In the OARO process, water permeates until the osmotic pressure difference ($\Delta\pi$) becomes equal to the applied pressure (ΔP). Thus, the maximum permeated water amount, V_{ideal} [L] can be calculated from initial concentration condition by considering the ideal separation without concentration polarization, pressure drop, and solute permeation through the membrane. By

using V_{ideal} [L] and the permeated water amount measured in the experiment,$V_{\mathrm{exp.}}$ [L], the module efficiency (η [%]) is defined by the following equation:

$$\eta = \frac{V_{\mathrm{exp.}}}{V_{\mathrm{ideal}}} \cdot 100. \tag{18}$$

3. Experimental

3.1. Materials and methods

For the concentration experiment using the OARO process, sodium chloride (NaCl) solution was used as a model solution. NaCl was analytical grade (purity > 99.5%) and was obtained from Wako Pure Chemical Industries (Osaka, Japan). The initial concentration of the solution was adjusted to 0.5 M or 1.0 M using tap water that had been purified with an activated carbon filter.

3.2. Hollow fiber membrane module

A 5-inch hollow fiber membrane module was provided by Toyobo (Osaka, Japan). The module was 58 cm long, had an inner diameter of 12 cm, and contained 216,720 hollow fiber membranes. This configuration gave a packing density of 54.2% and a membrane area of 76.8 m^2. The hollow fiber membranes were made from CTA, and had inner and outer diameters of 85 μm and 175 μm, respectively. The active layer with separation function faced the shell side, and the intrinsic membrane parameters such as water permeability coefficient (A), solute permeability coefficient (B), and structure parameter (S) were 0.27 $L \cdot m^{-2} \cdot h^{-1} \cdot bar^{-1}$, 0.035 $L \cdot m^{-2} \cdot h^{-1}$, and 1000 μm, respectively.[19] The hollow fiber membranes are cross-wound on a dispersion pipe.[21,25]

3.3. Pressure drop test

Pressure drop tests were carried out using the equipment shown in Fig. 5. Purified tap water was prepared in the shell side tank and the bore side tank. The shell side solution was supplied using a feed pump (MD-55FY, Iwaki, Japan) and a high-pressure pump (APP1.0, Danfoss, Japan), while the bore side solution was supplied using a low-pressure pump (CRN1-13, Grundfos, Japan). The feed solution temperature was controlled at 25 ± 1 °C with chiller units (RKE2200B1, Orion, Japan). Pressure drop tests were conducted with low flow rate (4.5 L/min) and high flow rate (8.0 L/min) at the shell side. The active layer of the membrane faced the shell side while the support layer faced the bore side. Because water should permeate from the shell side to the bore side, it was necessary to set the flow rate in such a way that the pressure on the shell side was always higher than the pressure on the bore side. Therefore, the bore side flow rate was changed from 3.0 to 4.5 L/min when the shell side flow rate was low (Q_{Shell} = 4.5 L/min), and was changed from 3.0 to 8.0 L/min when the shell side flow rate was high (Q_{Shell} = 8.0 L/min). The shell side and bore side pressures, flow rate, and temperature were recorded with a data logger (GL820-UM-801, Graphtec, Japan) connected to a computer.

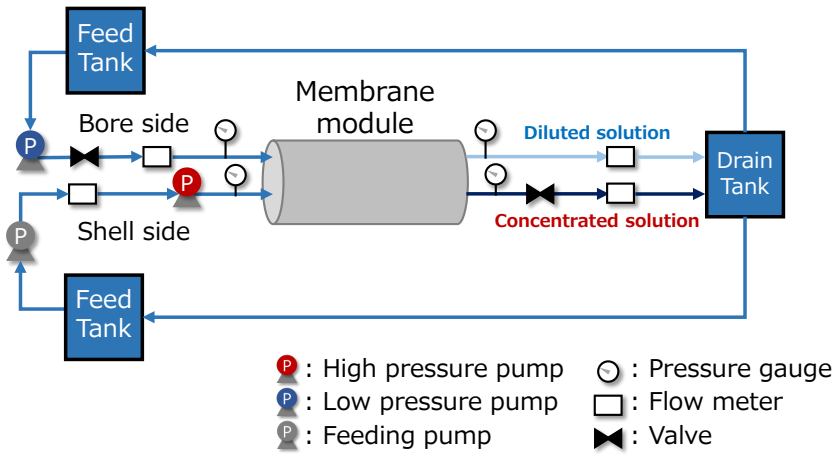

Figure 5 Schematic diagram of evaluation system.

3.4. Concentration test with OARO

Concentration tests using the OARO process were carried out using the equipment shown in Fig. 5. The initial concentrations of both the concentrated and diluted solutions were the same (0.5 M or 1.0 M). NaCl solution with the same concentration was prepared in the shell and bore side tanks, and electrical conductivity measurements (ES-71, Horiba, Japan) confirmed that the concentration remained constant. The active layer faced the shell side and water permeated from outside to inside the hollow fiber membranes by pressurizing the shell side. As a result, the shell side solution became concentrated and the bore side solution was diluted. The concentration of the shell side solution discharged from the module was measured with an electrical conductivity meter. The concentrated and diluted solutions were sent to a drain tank and returned to the shell side and bore side tanks using a circulation pump. The bore side flow rate was fixed at 3.5 L/min and the shell side flow rate was adjusted from 4.2 to 10.0 L/min. The pressure difference across the membrane was changed from 8 to 12 bar. The water flux was calculated by using Equation (8).

4. Results and discussion

4.1. Pure water flux and pressure drop

The pilot scale hollow fiber membrane module included a large number of hollow fibers with long effective length. Therefore, it was necessary to consider the pressure drops in the membrane module, which were affected by experimental conditions such as applied pressure and flow rates

in both the shell and bore sides. The effects of various operating conditions on the pressure drops in the membrane module were investigated using purified tap water. Figure 6 shows the effects of the shell side applied pressure on water flux (a, b) and the bore side pressure drop (c, d) when the bore side flow rate (Q_{Bore}) was changed from 3.0 to 8.0 L/min with the shell side flow rate (Q_{Shell}) set at 4.5 or 8.0 L/min. Generally, water flux increased with increased shell side applied pressure. Water flux decreased with increased bore side flow rate, Q_{Bore}, especially as shown in Fig. 6 (b). Figure 6 (c) and (d) show that the higher bore side flow rate led to a higher pressure drop ($\Delta P_{\mathrm{drop,Bore}}$). The bore side pressure at the module outlet was atmospheric pressure because the bore solution was exposed to the atmosphere, as shown in Fig. 5. Thus, the inlet bore side pressure increased with increased flow rate. This effect reduced the hydraulic pressure difference (= shell side pressure – bore side pressure) and therefore decreased the water flux. Thus, it was found that the bore side flow rate should be set as low as possible to reduce the pressure drop and to enhance the water flux.

As shown in Fig. 6 (c) and (d), the bore side pressure drop increased with increased shell side applied pressure. The higher applied pressure brought about higher water flux and higher bore side flow rate, which caused the pressure drop to increase.

The theoretical calculation results for the pure water flux and the bore side pressure drop are shown in Fig. 6 as solid lines. The calculated results were in good agreement with the experimental data under various operation conditions.

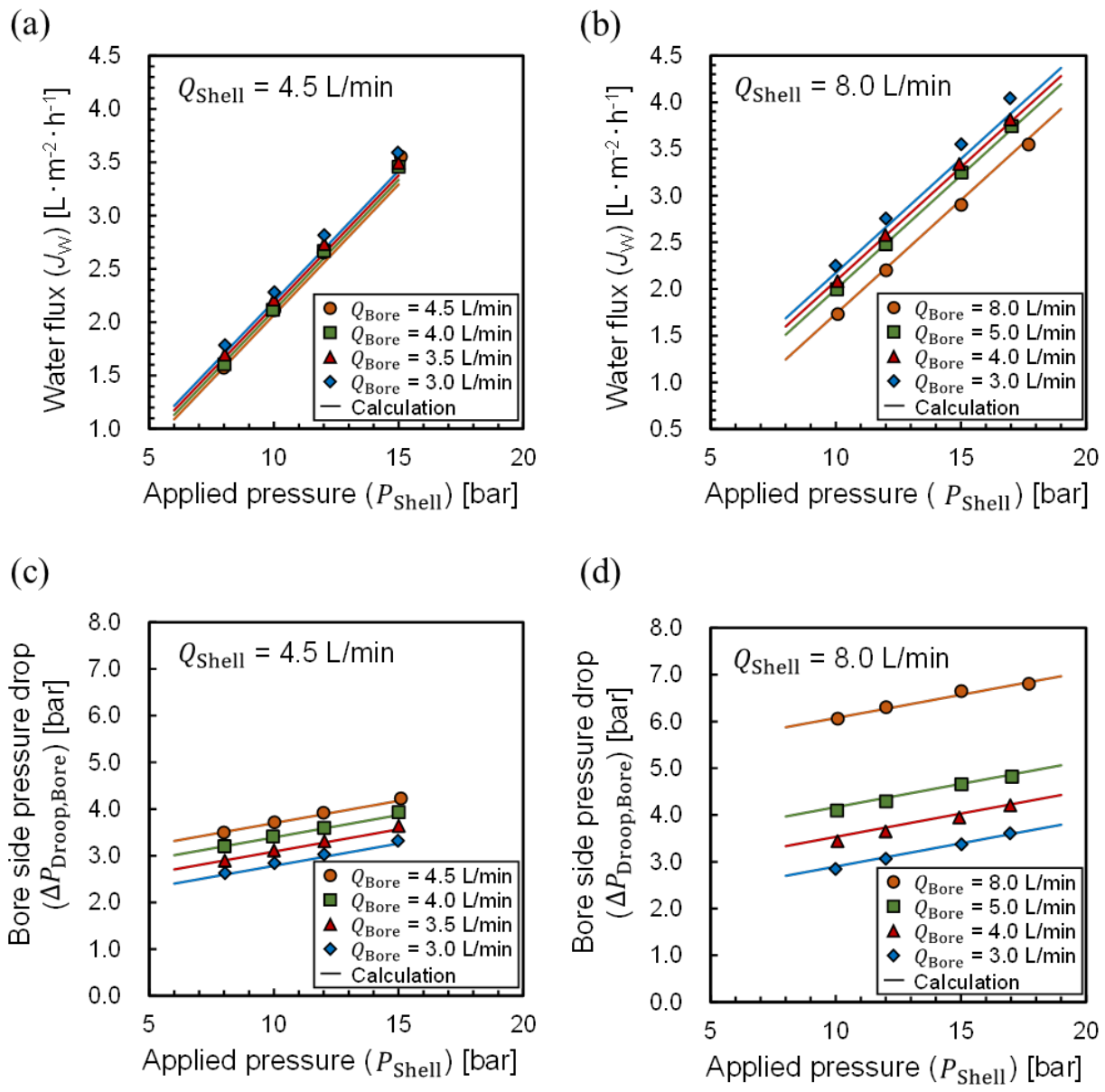

Figure 6 Effects of shell side pressure on water flux (a, b) and bore inlet pressure (c, d) when the bore side flow rate (Q_{Bore}) was changed: (a), (c) Q_{Shell} = 4.5 L/min and (b), (d) Q_{Shell} = 8.0 L/min. The purified tap water is used in this experiment.

4.2. Concentration test utilizing OARO process

Concentration tests were performed utilizing the OARO process with a bore side flow rate of 3.5 L/min. Figure 7 shows the changes of concentration for the concentrated side (a, b) and water flux (c, d) when the shell side flow rate (Q_{Shell}) was changed from 4.5 to 10.0 L/min and the applied pressure was changed from 8 to 12 bar (initial concentration of solution (C_0) = 0.5 or 1.0 M). The increase of concentration on the concentrated side was confirmed in this OARO process at any applied pressure and flow rate. These results demonstrate that use of the OARO process with low applied pressure allowed concentration of solution with high osmotic pressure up to 50 bar (1.0 M). The higher relative degree of concentration (concentration divided by initial concentration) was achieved in the case of lower initial solution concentration. In addition, the water flux was found to increase by increasing the shell side flow rate as shown in Fig.7 (c) and (d). These results are discussed in sections 4.3 and 4.4.

The theoretical calculation results for the change of concentration and water flux are shown in Fig. 7 as solid lines and are in good agreement with the experimental data under various operating conditions.

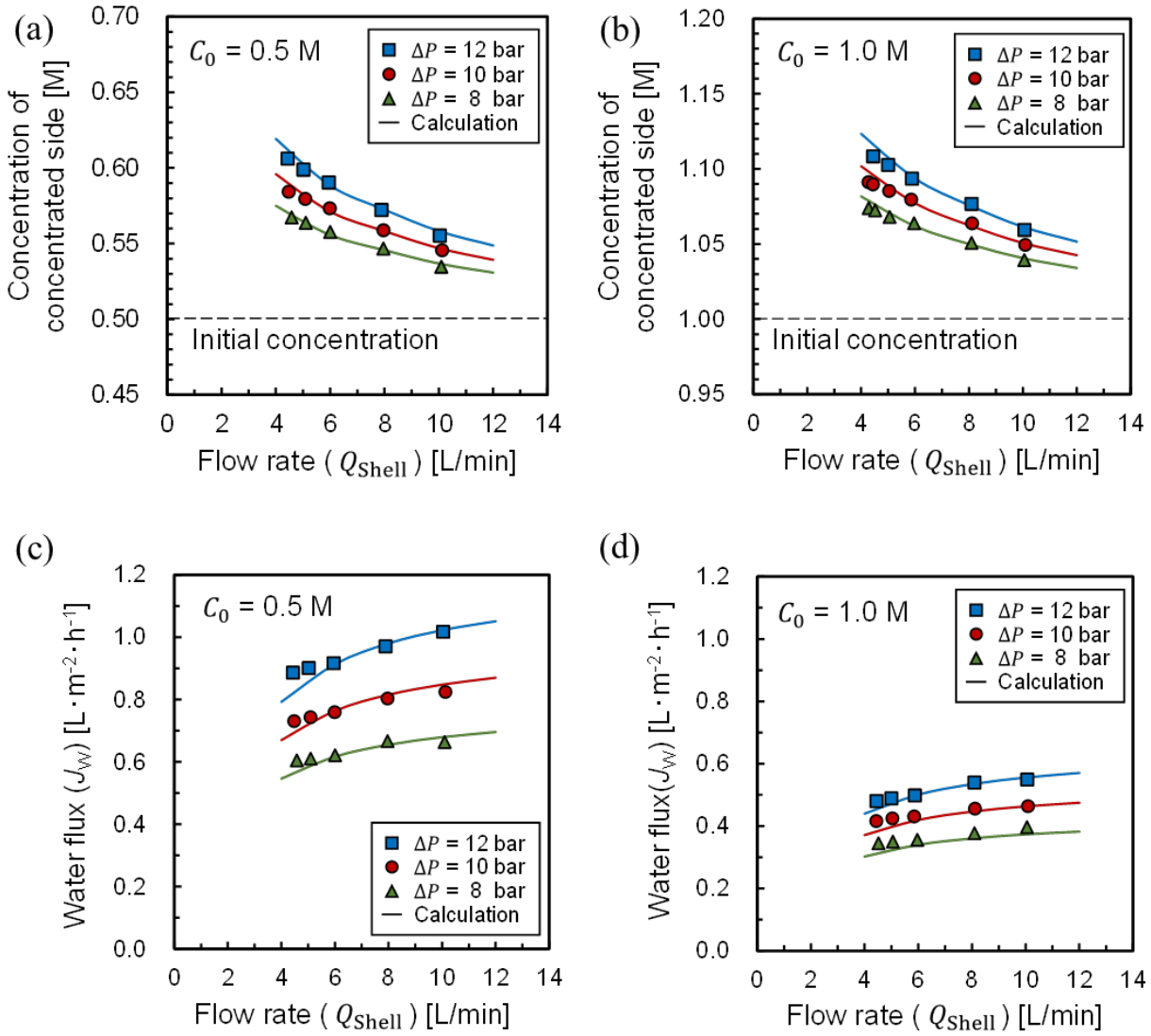

Figure 7 Results of concentration test utilizing OARO. Change of concentration of concentrated side (a, b) and water flux (c, d) against shell side flow rate. The initial concentration (C_0) was 0.5 M (a, c), and 1.0 M (b, d).

4.3. Effect of shell side flow rate on water flux

A difference in the concentration distribution is expected between the shell side and bore side because concentration occurs at the shell side and dilution occurs at the bore side toward the exit of the module. The difference of the concentration distribution may affect the water flux even though solution of the same concentration was supplied to both sides. To confirm the effect of the shell side flow rate on the water flux, the osmotic pressure distribution inside the module was calculated for different shell side flow rates (Q_{Shell} = 4.5 and 10.0 L/min), as shown in Fig. 8. The change in the osmotic pressure difference ($\Delta\pi_{\mathrm{bulk}}$) between the concentrated solution and the diluted solution in the module is shown using different colors. The applied pressure was 12 bar and the initial concentration was 0.5 M. The yellow and orange colored regions for high flow rate (Q_{Shell} = 10.0 L/min) were narrower than those for low flow rate (Q_{Shell} = 4.5 L/min), which indicates that the osmotic pressure difference for high flow rate was not high. This is because the residence time of the shell side solution in the module became shorter and the amount of the transported water was lower. This would explain why the water flux increased and the concentration on the concentrated side decreased by increasing the shell side flow rate (Fig.7 (c) and (d) and Fig. 7 (a) and (b)).

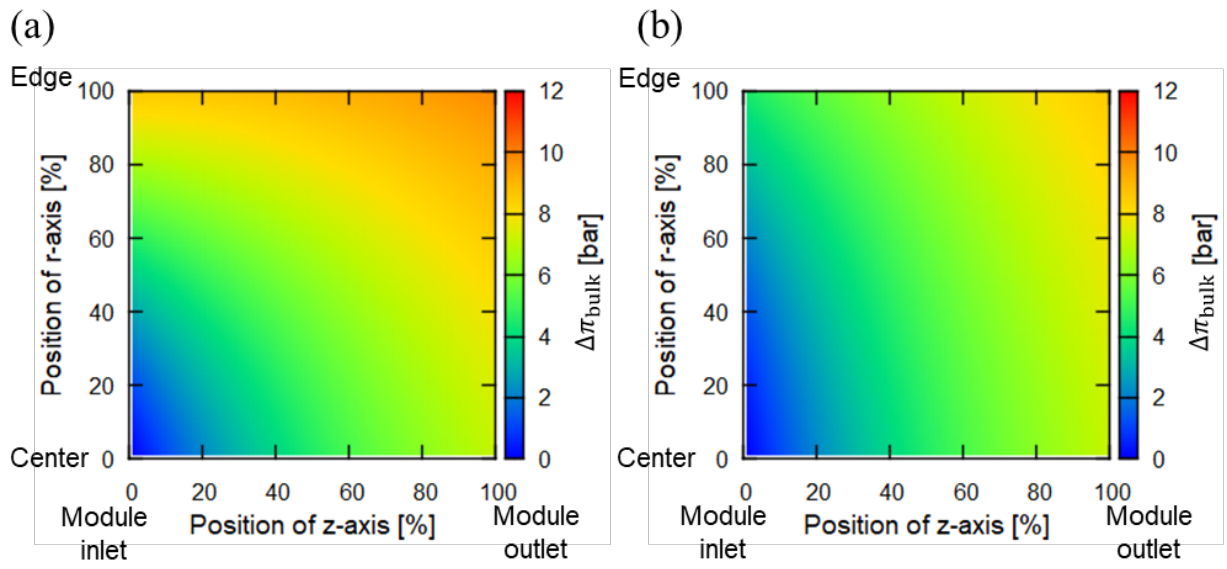

Figure 8 Osmotic pressure difference in module: (a) Q_{Shell} = 4.5 L/min and (b) Q_{Shell} = 10.0 L/min. Applied pressure, 12 bar; initial concentration, 0.5 M.

4.4. Effect of initial concentration of feed solution on up-concentration

As mentioned in section 2.1., ICP occurs in the support layer, leading to the decrease in the water flux. To confirm the effect of the initial concentration on the solution up-concentration, Δπ caused by ICP and apparent water permeability were calculated from Equation 2 in the case of without considering module dimension and are shown in Fig. 9. The applied pressure was 12 bar. The calculation was performed for the condition without bulk osmotic pressure difference ($\Delta\pi_{bulk}$) by equalizing the solution concentration between the shell side and the bore side. It was clear that Δπ caused by ICP increased and that apparent water permeability decreased with increasing concentration of the initial solution. At the beginning of this OARO process shown in Fig. 1 (a), the initial flux was the same regardless of the initial solution concentration because there was no

difference in the osmotic pressures between the shell and bore sides. Because of the same water flux, the initial dilution ratio in the support layer shown in Fig. 1 (b) was the same regardless of the solution concentration. Even in the case of the same dilution ratio, the absolute concentration decrease was higher in the case of the higher the initial solution concentration, although the relative concentration decrease was the same. Thus, Δπ caused by ICP became higher with increased initial solution concentration, which led to decreased water flux.

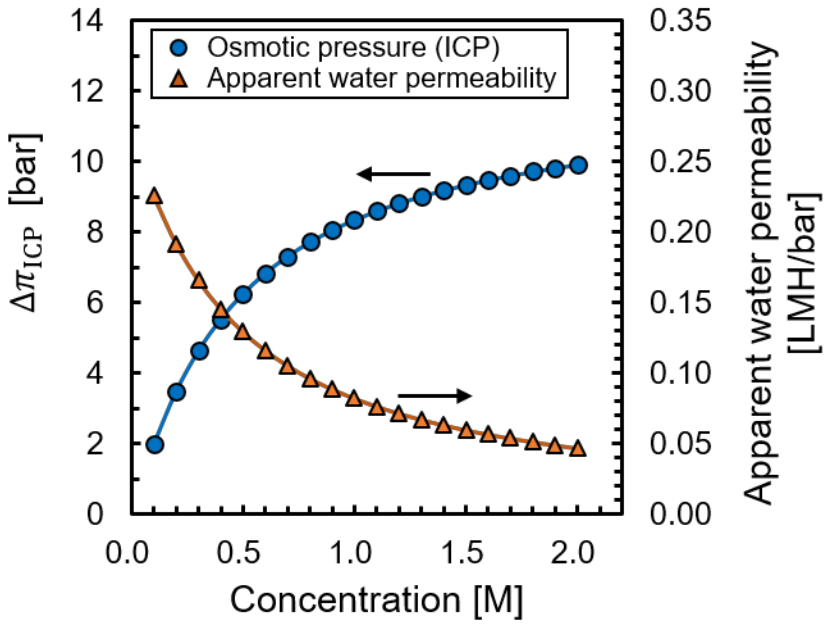

Figure 9 Relationship between concentration of feed solution and Δπ caused by ICP and apparent water permeability.

4.5. Evaluation of module efficiency (η)

Figure 10 shows the effects of the shell side flow rate on the module efficiency for initial feed solution concentrations of 0.5 and 1.0 M. There was a maximum value for module efficiency for

the shell side flow rate. In the low flow rate region, an increase in flow rate brought about a decrease in ECP. Therefore, module efficiency increased with increased flow rate. However, further increases in flow rate caused shorter residence time of the solution and decreased the amount of transported water as described in section 4.3. This raised the water permeation with low concentration on the concentrated side and high water flux, which led to lower module efficiency. Thus, it was apparent that an optimal flow rate existed for operation of the pilot scale hollow fiber membrane module. As mentioned in Section 2.4, this module efficiency is calculated from the volume change based on an ideal separation without concentration polarization, pressure drop, and solute permeation. On the other hand, a model which account for an effect of thermodynamics of electrolyte solution on salt transport has been recently proposed[26,27] It was reported that concentration polarization and thermodynamic non-ideality influenced salt transport coefficient in RO membrane.[27] Further investigation utilizing above model would be helpful to evaluate OARO process from the viewpoint of thermodynamic efficiency.

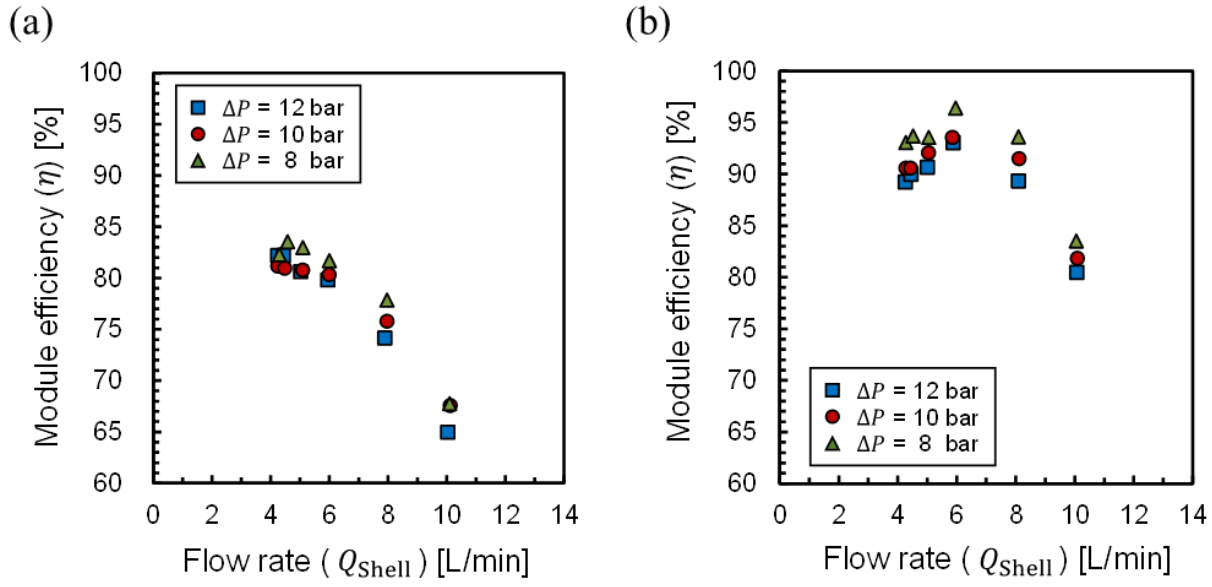

Figure 10 Results of module efficiency: (a) 0.5 M and (b) 1.0 M.

5. Conclusions

In this research, we performed concentration tests and theoretical calculations for the OARO process using a 5-inch CTA hollow fiber membrane module. Water permeation and solution concentration were achieved with applied pressure at 8–12 bar, even in the case of NaCl solution with high osmotic pressure ($\pi = 50$ bar). The water flux was observed to increase with increasing shell side flow rate. In addition, the effect of ICP decreased in the case of lower initial feed solution concentration, leading to the higher up-concentration. The evaluation of module efficiency found that a maximum value could be obtained and optimal operation conditions existed for the shell side flow rate. Furthermore, the calculation model for OARO performance was presented, and calculated results were in good agreement with the experimental results.

For realization of the OARO process, a high degree of concentration with appropriate separation membranes with less affected ICP are desirable to improve the concentration ratio and water flux. A multistage OARO process is another option to enhance concentration, and further work in this area is now in progress.

Corresponding Author

*Keizo Nakagawa, Tel & Fax: +81-78-803-6302, E-mail address: knakagaw@port.kobe-u.ac.jp

*Hideto Matsuyama, Tel & Fax: +81-78-803-6180, E-mail address: matuyama@kobe-u.ac.jp

Notes

The authors declare no competing financial interest.

Figure captions

Figure 1 Schematic diagram of the OARO process and concentration polarization, (a) without applied pressure, and (b) initial operating stage (left) and concentrated stage (right).

Figure 2 Schematic diagram of hollow fiber membrane module

Figure 3 (a) Division calculation method and (b) mass balance in small section

Figure 4 Effect of division number on water flux (Q_{Shell} = 4 L/min, ΔP = 12 bar, C_0 = 1.0 M)

Figure 5 Schematic diagram of evaluation system

Figure 6 Effects of shell side pressure on water flux (a, b) and bore inlet pressure (c, d) when the bore side flow rate (Q_{Bore}) was changed: (a), (c) Q_{Shell} = 4.5 L/min and (b), (d) Q_{Shell} = 8.0 L/min. The purified tap water is used in this experiment.

Figure 7 Results of concentration test utilizing OARO. Change of concentration of concentrated side (a, b) and water flux (c, d) against shell side flow rate. The initial concentration (C_0) was 0.5 M (a, c), and 1.0 M (b, d)

Figure 8 Osmotic pressure difference in module: (a) Q_{Shell} = 4.5 L/min and (b) Q_{Shell} = 10.0 L/min. Applied pressure, 12 bar; initial concentration, 0.5 M

Figure 9 Relationship between concentration of feed solution and $\Delta\pi$ caused by ICP and apparent water permeability

Figure 10 Results of module efficiency: (a) 0.5 M and (b) 1.0 M

References

(1) Wenten, I. G.; Khoiruddin. Reverse Osmosis Applications: Prospect and Challenges. *Desalination* **2016**, *391*, 112–125. https://doi.org/10.1016/j.desal.2015.12.011.

(2) Alvarez, V.; Alvarez, S.; Riera, F. A.; Alvarez, R. Permeate Flux Prediction in Apple Juice Concentration by Reverse Osmosis. *J. Membr. Sci.* **1997**, *127* (1), 25–34. https://doi.org/10.1016/S0376-7388(96)00285-2.

(3) Rodríguez, M.; Luque, S.; Alvarez, J. R.; Coca, J. A Comparative Study of Reverse Osmosis and Freeze Concentration for the Removal of Valeric Acid from Wastewaters. *Desalination* **2000**, *127* (1), 1–11. https://doi.org/10.1016/S0011-9164(99)00187-3.

(4) Madaeni, S. S.; Zereshki, S. Energy Consumption for Sugar Manufacturing. Part I: Evaporation versus Reverse Osmosis. *Energy Convers. Manag.* **2010**, *51* (6), 1270–1276. https://doi.org/10.1016/j.enconman.2010.01.002.

(5) Fritzmann, C.; Löwenberg, J.; Wintgens, T.; Melin, T. State-of-the-Art of Reverse Osmosis Desalination. **2007**, *216*, 1–76. https://doi.org/10.1016/j.desal.2006.12.009.

(6) Jesus, D. F.; Leite, M. F.; Silva, L. F. M.; Modesta, R. D.; Matta, V. M.; Cabral, L. M. C. Orange (Citrus Sinensis) Juice Concentration by Reverse Osmosis. *J. Food Eng.* **2007**, *81* (2), 287–291. https://doi.org/10.1016/j.jfoodeng.2006.06.014.

(7) Petrotos, K. B.; Lazarides, H. N. Osmotic Concentration of Liquid Foods. *J. Food Eng.* **2001**, *49* (2–3), 201–206. https://doi.org/10.1016/S0260-8774(00)00222-3.

(8) Jiao, B.; Cassano, A.; Drioli, E. Recent Advances on Membrane Processes for the Concentration of Fruit Juices: A Review. *J. Food Eng.* **2004**, *63* (3), 303–324. https://doi.org/10.1016/j.jfoodeng.2003.08.003.

(9) Park, K.; Kim, D. Y.; Yang, D. R. Cost-Based Feasibility Study and Sensitivity Analysis of a New Draw Solution Assisted Reverse Osmosis (DSARO) Process for Seawater Desalination. *Desalination* **2017**, *422* (August), 182–193. https://doi.org/10.1016/j.desal.2017.08.026.

(10) Chen, X.; Yip, N. Y. Unlocking High-Salinity Desalination with Cascading Osmotically Mediated Reverse Osmosis: Energy and Operating Pressure Analysis. *Environ. Sci. Technol.* **2018**, *52* (4), 2242–2250. https://doi.org/10.1021/acs.est.7b05774.

(11) Kim, J.; Kim, J.; Kim, J.; Hong, S. Osmotically Enhanced Dewatering-Reverse Osmosis (OED-RO) Hybrid System: Implications for Shale Gas Produced Water Treatment. *J. Membr. Sci.* **2018**, *554*, 282–290. https://doi.org/10.1016/j.memsci.2018.03.015.

(12) Kim, J.; Kim, D. I.; Hong, S. Analysis of an Osmotically-Enhanced Dewatering Process for the Treatment of Highly Saline (Waste)Waters. *J. Membr. Sci.* **2017**, *548*, 685–693. https://doi.org/10.1016/j.memsci.2017.10.048.

(13) Bartholomew, T. V.; Mey, L.; Arena, J. T.; Siefert, N. S.; Mauter, M. S. Osmotically Assisted Reverse Osmosis for High Salinity Brine Treatment. *Desalination* **2017**, *421*, 3–11. https://doi.org/10.1016/j.desal.2017.04.012.

(14) Kim, Y. C.; Park, S. J. Experimental Study of a 4040 Spiral-Wound Forward-Osmosis Membrane Module. *Environ. Sci. Technol.* **2011**, *45* (18), 7737–7745. https://doi.org/10.1021/es202175m.

(15) Xu, Y.; Peng, X.; Tang, C. Y.; Fu, Q. S.; Nie, S. Effect of Draw Solution Concentration and Operating Conditions on Forward Osmosis and Pressure Retarded Osmosis Performance in a Spiral Wound Module. *J. Membr. Sci.* **2010**, *348* (1–2), 298–309. https://doi.org/10.1016/j.memsci.2009.11.013.

(16) Goosen, M. F. A.; Sablani, S. S.; Al-Maskari, S. S.; Al-Belushi, R. H.; Wilf, M. Effect of Feed Temperature on Permeate Flux and Mass Transfer Coefficient in Spiral-Wound Reverse Osmosis Systems. *Desalination* **2002**, *144* (1–3), 367–372. https://doi.org/10.1016/S0011-9164(02)00345-4.

(17) Kim, J.; Blandin, G.; Phuntsho, S.; Verliefde, A.; Le-Clech, P.; Shon, H. Practical Considerations for Operability of an 8″ Spiral Wound Forward Osmosis Module: Hydrodynamics, Fouling Behaviour and Cleaning Strategy. *Desalination* **2017**, *404*, 249–258. https://doi.org/10.1016/j.desal.2016.11.004.

(18) Higa, M.; Shigefuji, D.; Shibuya, M.; Izumikawa, S.; Ikebe, Y.; Yasukawa, M.; Endo, N.; Tanioka, A. Experimental Study of a Hollow Fiber Membrane Module in Pressure-Retarded Osmosis: Module Performance Comparison with Volumetric-Based Power Outputs. *Desalination* **2017**, *420*, 45–53. https://doi.org/10.1016/j.desal.2017.06.015.

(19) Shibuya, M.; Yasukawa, M.; Goda, S.; Sakurai, H.; Takahashi, T.; Higa, M.; Matsuyama, H. Experimental and Theoretical Study of a Forward Osmosis Hollow Fiber Membrane

Module with a Cross-Wound Configuration. *J. Membr. Sci.* **2016**, *504*, 10–19. https://doi.org/10.1016/j.memsci.2015.12.040.

(20) Tanaka, Y.; Yasukawa, M.; Goda, S.; Sakurai, H.; Shibuya, M.; Takahashi, T.; Kishimoto, M.; Higa, M.; Matsuyama, H. Experimental and Simulation Studies of Two Types of 5-Inch Scale Hollow Fiber Membrane Modules for Pressure-Retarded Osmosis. *Desalination* **2018**, *447*, 133–146. https://doi.org/10.1016/j.desal.2018.09.015.

(21) Kumano, A.; Marui, K.; Terashima, Y. Hollow Fiber Type PRO Module and Its Characteristics. *Desalination* **2016**, *389*, 149–154. https://doi.org/10.1016/j.desal.2016.01.001.

(22) McCutcheon, J. R.; Elimelech, M. Influence of Concentrative and Dilutive Internal Concentration Polarization on Flux Behavior in Forward Osmosis. *J. Membr. Sci.* **2006**, *284* (1–2), 237–247. https://doi.org/10.1016/j.memsci.2006.07.049.

(23) Tan, C. H.; Ng, H. Y. Modified Models to Predict Flux Behavior in Forward Osmosis in Consideration of External and Internal Concentration Polarizations. *J. Membr. Sci.* **2008**, *324* (1–2), 209–219. https://doi.org/10.1016/j.memsci.2008.07.020.

(24) Suh, C.; Lee, S. Modeling Reverse Draw Solute Flux in Forward Osmosis with External Concentration Polarization in Both Sides of the Draw and Feed Solution. *J. Membr. Sci.* **2013**, *427*, 365–374. https://doi.org/10.1016/j.memsci.2012.08.033.

(25) Sekino, M. Precise Analytical Model of Hollow Fiber Reverse Osmosis Modules. *J. Membr. Sci.* **1993**, *85* (3), 241–252. https://doi.org/10.1016/0376-7388(93)85278-5.

(26) Mickols, W. Substantial changes in the transport model of reverse osmosis and nanofiltration by incorporating accurate activity data of electrolytes, *Ind. Eng.Chem. Res.* **2016**, *55*, 11139–11149. https://pubs.acs.org/doi/10.1021/acs.iecr.6b03248.

(27) Jang, E-S.; Mickols, W.; Sujanani, R.; Helenic, A.; Dilenschneider, T. J.; Kamcev, J.; Paul, D. R.; Freeman, B. D. Influence of concentration polarization and thermodynamic non-ideality on salt transport in reverse osmosis membranes, *J. Membr. Sci.* **2019**, *572*, 668–675. https://doi.org/10.1016/j.memsci.2018.11.006